AGU PUBLICATIONS

Geochemistry, Geophysics, Geosystems

RESEARCH ARTICLE
10.1002/2015GC005950

Focusing of upward fluid migration beneath volcanic arcs: Effect of mineral grain size variation in the mantle wedge

Ikuko Wada[1] and Mark D. Behn[2]

[1]Department of Earth Sciences, University of Minnesota, Minneapolis, Minnesota, USA, [2]Department of Geology and Geophysics, Woods Hole Oceanographic Institution, Woods Hole, Massachusetts, USA

Key Points:
- Effect of grain size variation is incorporated into fluid migration models of subduction zones
- Fluids are dragged downdip by corner flow due to fine grain size immediately above the slab
- Fore-arc downdip migration and back-arc trench-ward migration focus fluids beneath the arc

Supporting Information:
- Supporting Information S1

Correspondence to:
I. Wada,
iwada@umn.edu

Citation:
Wada, I., and M. D. Behn (2015), Focusing of upward fluid migration beneath volcanic arcs: Effect of mineral grain size variation in the mantle wedge, *Geochem. Geophys. Geosyst.*, *16*, 3905–3923, doi:10.1002/2015GC005950.

Received 5 JUN 2015
Accepted 13 OCT 2015
Accepted article online 19 OCT 2015
Published online 13 NOV 2015

Abstract We use numerical models to investigate the effects of mineral grain size variation on fluid migration in the mantle wedge at subduction zones and on the location of the volcanic arc. Previous coupled thermal-grain size evolution (T-GSE) models predict small grain size (<1 mm) in the corner flow of the mantle wedge, a downdip grain size increase by ~2 orders of magnitude along the base of the mantle wedge, and finer grain size in the mantle wedge for colder-slab subduction zones. We integrate these T-GSE modeling results with a fluid migration model, in which permeability depends on grain size, and fluid flow through a moving mantle matrix is driven by fluid buoyancy and dynamic pressure gradients induced by mantle flow. Our modeling results indicate that fluids introduced along the base of the mantle wedge beneath the fore arc are initially dragged downdip by corner flow due to the small grain size and low permeability immediately above the slab. As grain size increases with depth, permeability increases, resulting in upward fluid migration. Fluids released beneath the arc and the back arc are also initially dragged downdip, but typically are not transported as far laterally before they begin to travel upward. As the fluids rise through the back-arc mantle wedge, they become deflected toward the trench due to the effect of mantle inflow. The combination of downdip migration in the fore arc and trench-ward migration in the back arc results in pathways that focus fluids beneath the arc.

1. Introduction

In subduction zones, the motion of the subducting slab drives solid-state mantle flow in the overlying mantle wedge (Figure 1a) [*McKenzie*, 1969]. The flow replenishes the mantle wedge with hot mantle, providing the thermal conditions necessary for melt generation and arc volcanism. Numerical models of subduction zone thermal structure predict a wide region of relatively high temperatures (>1000°C) in the flowing part of the mantle wedge, extending from slightly trench-ward of the arc into the back-arc region [e.g., *Furukawa*, 1993; *van Keken et al.*, 2002; *Currie et al.*, 2004; *Wada and Wang*, 2009; *Syracuse et al.*, 2010]. A series of dehydration reactions occur in the subducting slab at various depths, dictated by the thermal structure of the slab [*Peacock*, 1990; *Pawley and Holloway*, 1993; *Schmidt and Poli*, 1998; *Hacker et al.*, 2003; *Hacker*, 2008; *van Keken et al.*, 2011]. Aqueous fluids released from the dehydrating slab migrate into the overlying mantle wedge to cause hydrous melting and arc volcanism [e.g., *Mysen and Boettcher*, 1975; *Gaetani and Grove*, 1998; *Schmidt and Poli*, 1998; *Ulmer*, 2001; *Grove et al.*, 2006]. Given that relatively high temperatures are maintained over a wide region in the mantle wedge and that aqueous fluids are released at various depths, melt generation and arc volcanism are expected to occur over a wide region. However, surficial arc volcanism tends to occur in a relatively narrow region overlying the location where the slab reaches a depth of 80–120 km and appears to have little correlation with the depth of fluid release from the slab [*England et al.*, 2004; *Syracuse and Abers*, 2006; *van Keken et al.*, 2011]. Thus, one of the outstanding questions in the studies of subduction zone processes is the mechanism that controls the location of the arc across different subduction zones with widely varying slab thermal structures.

A range of mechanisms have been proposed to focus aqueous fluids and melts beneath the arc and to explain the relatively uniform location of the arc with respect to the slab surface depth (Figure 1a). These mechanisms include the pressure-dependent dehydration reaction of amphibole [*Tatsumi*, 1986], a complex sequence of dehydration and hydration reactions [*Davies and Stevenson*, 1992], the breakdown of chlorite [*Grove et al.*, 2009], and anhydrous melting [*England and Katz*, 2010] in the mantle wedge. In all of these models, water is bound in hydrous phases and is transferred both downdip and laterally through advection with the flowing mantle.

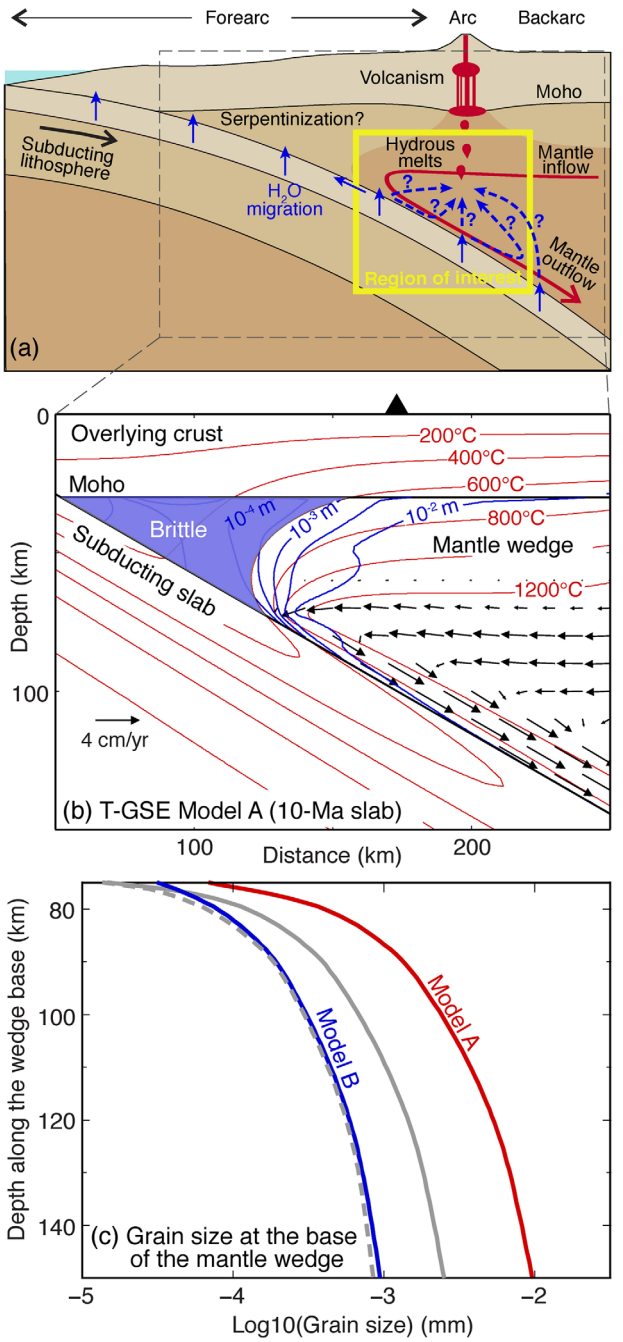

Figure 1. (a) Schematic illustration of potential fluid migration paths and melt generation in the mantle wedge at subduction zones. (b) Thermal field (red contours), mantle velocities (black arrows), and grain size distribution (blue contours) calculated by T-GSE Model A. T-GSE modeling results are not applicable to the region with temperature <600°C (purple region) in the mantle wedge. (c) Grain size variation along the base of the mantle wedge just above the top of the slab predicted by T-GSE Models A and B (red and blue lines, respectively). The grain size distributions calculated by the T-GSE model for a 30 Ma slab with a subduction rate of 4 cm/yr (solid grey line) and a 100 Ma slab with a subduction rate of 8 cm/yr (dashed grey line) are also shown.

In addition, water can be transported as a free fluid. In the lithosphere, fluids likely migrate through a network of fractures and faults, but in the hot mantle wedge, the primary fluid passage is interconnected pores between mineral grains with a wetting angle of <60° [*Mibe et al.*, 1999]. One of the important factors that affect the path of porous flow is the permeability of the mantle wedge. Experimental observations indicate that permeability is proportional to the cube of fluid fraction and the square of grain size [*Wark and Watson*, 1998; *Wark et al.*, 2003; *Miller et al.*, 2014]. The strong dependence of permeability on fluid fraction and grain size therefore affects the migration of aqueous fluids and melt.

Several numerical studies have investigated fluid migration in the mantle wedge, focusing on different factors that affect fluid migration and melt generation [e.g., *Iwamori*, 1998, 2007; *Cagnioncle et al.*, 2007; *Hebert et al.*, 2009; *Hebert and Montési*, 2013; *Wilson et al.*, 2014]. In the model of *Cagnioncle et al.* [2007], fluid flow is controlled by the competition between the buoyancy of fluids and the mantle velocity. Specifically, they showed that if the grain size in the mantle wedge is varied from a uniform value of 1 to 0.3 mm (at a constant fluid influx), the fluid/melt migration paths change from dominantly upward to primarily downdip due to change in the permeability—indicating the important role of grain size in controlling the fluid migration path. However, while all fluid flow studies to date, including those that incorporate the effects of melting in the mantle wedge [*Iwamori*, 1998, 2007; *Hebert et al.*, 2009] and dynamic pressure gradients induced by mantle compaction [*Wilson et al.*, 2014], have assumed a uniform grain size, it is known that grain size should evolve with varying thermal and deformation conditions in the mantle [e.g., *Hall and Parmentier*, 2003; *Wada et al.*, 2011; *Turner et al.*, 2015].

Grain size evolution is controlled by the competition between grain growth and grain size reduction due to dynamic recrystallization [*Karato*, 1984]. *Wada et al.* [2011] estimated the distribution of grain size in the mantle wedge, by coupling a subduction zone thermal model with the grain size evolution model (GSE) of *Austin and Evans* [2007]. Their modeling

results indicate that grain size at the base of the mantle wedge increases from 10–100 μm at $\sim$75 km depth to a few millimeters to a few centimeters at subarc depth (Figures 1b and 1c). Thus, because an increase in grain size by 2 orders of magnitude can lead to an increase in permeability by 4 orders of magnitude, variations in grain size must be considered when evaluating fluid migration pathways in the mantle wedge.

In this study, we develop a fluid migration model that incorporates a spatially variable grain size field and investigate its effect on the migration of aqueous fluids in the mantle wedge of subduction zones. Grain size, mantle flow velocities, dynamic pressure gradients, and temperature in the mantle wedge are calculated using the coupled thermal-grain size evolution (T-GSE) model of *Wada et al*. [2011]. Fluid migration is then driven through the resulting grain size field due to a combination of buoyancy, mantle flow, and dynamic pressure gradients induced by the mantle flow. We neglect the effects of compaction and melting and focus on the effects of grain size in controlling fluid migration paths. We test the model with different spatial patterns of fluid influx to the mantle wedge, first using a simple Gaussian influx pattern and then more realistic influx patterns calculated based on the slab thermopetrologic structure. Through the analyses of the modeling results, we explore their implications for the distribution of aqueous fluids in the mantle wedge and the locations of hydrous melting and arc volcanism.

2. Modeling Approach

2.1. Coupled Thermal-Grain Size Evolution (T-GSE) Model Setup

We use the coupled T-GSE model of *Wada et al*. [2011] to calculate the distribution of grain size in the mantle wedge. This approach utilizes a 2-D finite element code PGCtherm2D, which has been benchmarked with several other codes for subduction zone thermal modeling [*van Keken et al*., 2008]. The model consists of a nondeforming overlying crust, a subducting slab with kinematically prescribed velocity, and a viscous mantle wedge. Viscous coupling between the subducting slab and the overlying mantle wedge that induces mantle wedge flow in the model is controlled by the viscosity of a thin layer that is imposed along the plate interface to represents the strength of the plate interface. The interface strength is adjusted such that the slab and the mantle are fully coupled at $>$75 km depth to be consistent with the relatively uniform decoupling depth inferred globally [*Wada and Wang*, 2009; *Syracuse et al*., 2010]. The coupled T-GSE model calculates the 2-D steady state temperature field within the entire model domain and the deformation condition and grain size distribution in the mantle wedge that are in equilibrium with temperature.

For the calculation of the grain size distribution, the model adopts the GSE "wattmeter" model of *Austin and Evans* [2007], which is based on the premise that the rate of change in grain size is controlled by two competing processes, static grain growth and grain recrystallization. The former is largely temperature dependent, while the latter depends on deformation condition (stress and strain rate), which is coupled to temperature through the mantle rheology. Our parameterization of the GSE model is calibrated to fit laboratory data on grain size change of olivine [*Behn et al*., 2009]. The GSE model does not explicitly include the effect of grain boundary pinning [*Evans et al*., 2001], in which secondary phases such as pyroxene and spinel limit the maximum extent of grain growth by pinning the grain boundary. We approximate the effect of grain boundary pinning by imposing the maximum extent of grain growth of 3 cm in the T-GSE model.

For the mantle wedge, we use a composite mantle rheology that accounts for both grain-size-dependent diffusion and grain-size-independent dislocation creep with rheological parameters determined for wet olivine [*Hirth and Kohlsted*, 2003; *Behn et al*., 2009]. It was found, however, that the effect of grain size on the mantle rheology is small because dislocation creep dominates the deformation in the creeping part of the mantle wedge [*Wada et al*., 2011].

Following *Wada et al*. [2011], we adopt a generic model geometry, which consists of a 35 km-thick overlying crust and a 95 km-thick slab with a 30° constant dip (Figure 1b). The thermal structure of the slab affects temperature and deformation conditions in the overlying mantle wedge, particularly near the slab-mantle interface, and is an important factor that controls grain size. Slab age and subduction rate are the dominant parameters that influence subduction zone thermal structure. Thus, in T-GSE Models A and B, we investigate scenarios with a 10 and 100 Ma slab, respectively, and a subduction rate of 4 cm/yr (Figure 1b; Table 1).

Table 1. T-GSE Model Parameters

T-GSE Model	Slab Age (Ma)	Subduction Rate (cm/yr)	*b* (mm) at a Given Depth		
			75 km	80 km	100 km
A	10	4	0.081	0.436	2.470
B	100	4	0.035	0.083	0.315

Another factor that influences the thermal structure is the trench-ward extent of solid-state mantle wedge flow, which is driven largely by viscous coupling between the slab and the overlying mantle. The degree of coupling depends on the strength contrast between the slab-mantle interface and the overlying mantle [*Wada et al*., 2008]. In the T-GSE model, we use a thin viscous layer to represent the strength of the slab-mantle interface as in *Wada et al*. [2011], and we assign a layer viscosity such that the slab and the overlying mantle are fully coupled at depths >75 km, consistent with global studies on the depth of slab-mantle viscous coupling [*Wada and Wang*, 2009; *Syracuse et al*., 2010]. At depths <75 km, the overlying mantle is decoupled from the slab and is nearly completely stagnant and cold. Because our T-GSE model does not account for grain size change caused by brittle deformation, only the calculated grain size distribution in the creeping part of the mantle wedge is considered meaningful. Thus, in our fluid migration model, we discuss the T-GSE modeling results for the creeping regions only, which are approximated by regions where temperatures are 600°C or higher.

2.2. Fluid Migration (FM) Model Setup

We next develop a fluid migration (FM) model using the commercial finite element package COMSOL Multiphysics, which has been benchmarked along with PGCtherm2D used for the T-GSE model in the study by *van Keken et al*. [2008]. In this study, we do not make distinctions among different types of fluids (e.g., aqueous fluids and melts) and assume that they collectively have constant physical properties. The conservation of mass for the fluid phase is expressed by

$$\frac{\partial \phi}{\partial t} = -\nabla \cdot \left[\vec{V}_f \phi\right] \tag{1}$$

where ϕ is fluid volume fraction and $\vec{V}_f$ is fluid velocity. Fluid velocity is the sum of the mantle flow velocity ($\vec{V}_m$) and the fluid velocity relative to the mantle matrix,

$$\vec{V}_f = \vec{V}_m + \frac{\vec{S}}{\phi} \tag{2}$$

where $\vec{S}$ is Darcy velocity

$$\vec{S} = -\frac{k}{\eta}\left[\Delta\rho\vec{g} + \nabla P\right] = -\frac{k}{\eta}\vec{f} \tag{3}$$

Here k is permeability, η is fluid viscosity, $\Delta\rho$ is density difference between the mantle matrix and fluid, $\vec{g}$ is gravity, and P is dynamic pressure. In this study, we include dynamic pressure gradients caused by mantle flow, but dynamic pressure gradients caused by matrix compaction are not included. The total driving force for fluid flow ($\vec{f}$) is then the sum of the buoyancy of the fluid and pressure gradients due to mantle shear.

A relation among permeability, fluid fraction, and grain size b of rocks is commonly expressed as

$$k = \frac{b^2 \phi^n}{C} \tag{4}$$

where C is a geometrical factor. The empirically derived value of the fluid fraction exponent n ranges from 1 to 3 [*Riley and Kohlstedt*, 1991; *Wark and Watson*, 1998; *Wark et al*. 2003; *Zhu and Hirth*, 2003]. Both values of n and C depend on a number of factors, such as mineral composition and dihedral angle, and the choice of their values in our model influences the simulation results. For example, as seen from equations (3) and (4), for a given initial porosity permeability and thus Darcy velocity are greater for smaller n, affecting the evolution of fluid migration paths. This trend was clearly observed from a suite of modeling results that we obtained for a range of n and C values. However, for any choice of n and C within their reported ranges, fluid migration patterns that are similar to those presented in sections 3 and 4 can be obtained by varying the fluid influx and the time scale of model simulation. Thus, to investigate the first-order effect of grain size variation, we choose $n = 3$ and $C = 270$ as reported by *Wark et al*. [2003] for texturally equilibrated melt-bearing quartzites, whose pore geometries are analogous to those of upper mantle rocks.

Substituting equations (2)−(4) into equation (1) and casting it into partial differential form, we obtain

$$\frac{\partial\phi}{\partial t}+\left(V_{mx}-\frac{f_x}{\eta}\frac{dk}{d\phi}\right)\frac{\partial\phi}{\partial x}+\left(V_{my}-\frac{f_y}{\eta}\frac{dk}{d\phi}\right)\frac{\partial\phi}{\partial y}-\left(\frac{\partial\nabla P_x}{\partial x}+\frac{\partial\nabla P_y}{\partial y}\right)\frac{k}{\eta}=0 \tag{5}$$

The last term on the left-hand side of equation (5) is small and is neglected in our model. The steady state grain size distribution, mantle velocity, and dynamic pressure gradients calculated from the coupled T-GSE model are held constant throughout the FM models unless otherwise stated. Given large uncertainties and variations in the density and viscosity of fluids and lack of constraints on fluid influx and time scale of fluid migration, we consider fluids with constant physical properties ($\Delta\rho = 2000$ kg/m^3 and $\eta = 1$ Pa s). The systematic trade-offs between η and ϕ is discussed in section 3.1.1. Equation (5) is solved for ϕ using the PDE coefficient form application mode of COMSOL Multiphysics, defined as

$$\frac{\partial\phi}{\partial t}+\beta\cdot\nabla\phi+\nabla\cdot(-c\nabla\phi)=0 \tag{6}$$

where β is the convection coefficient $\left(\beta=\left[\left(V_{mx}-\frac{f_x}{\eta_f}\frac{dk}{d\phi}\right),\left(V_{my}-\frac{f_y}{\eta_f}\frac{dk}{d\phi}\right)\right]\right)$ and c is the diffusion coefficient. Ideally for our problem, $c = 0$. However, the Galerkin finite element discretization method generates unstable solutions for advection-dominated problems (defined as those with elemental Peclet number ($\beta h/2c$) > 1 where h is element size), leading to spurious oscillations. To stabilize the solution, we add an artificial isotropic diffusion that is scaled with the norm of β, $||\beta||$, and defined as

$$c=\delta||\beta||h/2p \tag{7}$$

where δ is a tuning parameter, and p is the order of the interpolation function ($p = 2$ for quadratic elements used in our model). When $\delta = 1$, the Peclet number is around 1.

To find the element size distribution and the δ value that minimize the artificial diffusion while keeping the computational time reasonable, we performed a series of tests varying h and δ (supporting information). We find that $\delta = 0.25$ and the mesh construction (Mesh 2) shown in supporting information Figure S1b results in negligibly small effects of artificial diffusion and reasonable computational time without producing numerical instability. Thus, we use $\delta = 0.25$ and Mesh 2 in all FM models presented below except FM Models III–V, in which Mesh 2 is modified to have finer mesh in the wedge corner without a modification to the δ value.

The FM model domain comprises only the mantle wedge, whose geometry is consistent with that of the coupled T-GSE model with the slab dip (θ) of 30° as described in section 2.1 (Figure 1b). The effect of steeper slab dip of 60° on grain size distribution was investigated by *Wada et al*. [2011], and the results show that the rate of an increase in grain size with depth at the base of the mantle wedge is comparable to those with 30° slab dip. Given the similar rates of grain size increase with depth, the vertical distance over which fluids are dragged by the mantle flow is expected to be similar for slabs with similar thermal states, but the horizontal distance of downdip drag becomes shorter for steeper dip due to the geometrical effect.

The updip end of the creeping region, where grain size calculations yield meaningful results (section 2.1), coincides approximately with the slab-mantle coupling depth (~75 km). Below this depth along the base of the mantle wedge, we apply a Dirichlet boundary condition,

$$\phi=\phi_0 \tag{8}$$

where ϕ_0 is a predefined function of depth as will be further described below, and simulate the effect of fluid influx. On all other segments of the model boundaries, we impose a zero-influx condition,

$$-\vec{n}\cdot(-c\nabla\phi)=0 \tag{9}$$

where $\vec{n}$ is the outward-pointing unit normal vector, while porosity can freely advect out across them. The porosity inside the model domain is initially set to zero. We do not consider fluid influx at depths shallower than the updip end of the creeping region where temperatures of the mantle wedge fall below the brittle-ductile transition. The amount of water that can be bound in nominally anhydrous minerals in the creeping region is assumed to be negligible compared to the amount of influx.

As discussed above, fluid fraction affects permeability (equation (4)), and therefore the pattern of fluid influx (ϕ_0) at the base of the mantle wedge, is another important factor that controls the fluid migration pattern.

Table 2. FM Models With a Uniform Grain Size Distribution Shown in Figures

FM Model	Grain Size (mm)	Influx Pattern	Figure
I	1	$y_0 = 100$ km	2
II	1	$y_0 = 100$ km	2
III	1	$y_0 = 80$ km	4
IV	1	$y_0 = 100$ km	4
V	1	Thermopetrologically consistent influx pattern	7
VI	10	Thermopetrologically consistent influx pattern	7

We use two approaches to quantify the effect of fluid influx on fluid migration for a given grain size distribution. One approach is to impose fluid influx over an isolated depth range and examine how the fluid migration path evolves. For the fluid influx, we assume a Gaussian distribution for fluid influx defined as

$$\phi_0(y) = \bar{\phi}_0 \exp\left(-\frac{(y-y_0)^2}{2\sigma^2}\right) \quad (10)$$

where $\bar{\phi}_0$ is the fluid fraction at the peak fluid influx centered at $y = y_0$ along the base of the mantle wedge with a characteristic width parameter $\sigma = 500$ m. The other approach is to apply a fluid influx distribution calculated from the thermopetrologic model of *Wada et al.* [2012]. The details of this approach are discussed in section 4.

Melt generation due to addition of aqueous fluids into the hot region of the mantle wedge may play an important role in controlling the subsequent migration paths of fluids to the surface as it increases the density, viscosity, and fraction of fluids. Increased density and viscosity are likely to slow the ascent of fluids whereas increased fluid fraction leads to higher permeability and facilitates fluid migration. While these are important factors that affect fluid migration paths, we simplified the problem by excluding the effect of melting and use a uniform fluid density and viscosity to study the first-order effect of grain size variation on fluid migration. Further, we assume that fluid migration through the lithospheric part of the mantle wedge and the overlying crust is predominantly vertical (facilitated by brittle processes), and therefore the horizontal location of fluids at the top of the mantle wedge roughly corresponds to the location of arc at the surface.

2.2.1. FM Model Naming Conventions

In the following sections, we use Roman numerals, I–VI, to refer to FM models with uniform grain sizes (Table 2). The previous T-GSE modeling results of *Wada et al.* [2011] indicate that the dominant deformation mechanism in the creeping region is dislocation creep, which is independent of grain size. This implies that the variations in grain size calculated from the T-GSE model have a negligible effect on the resulting mantle flow field and dynamic pressure gradients. Thus, although the grain size is assumed to be uniform in FM Models I–VI, we continue to adopt the mantle velocity field and dynamic pressure gradients calculated by T-GSE Model A. Further, the application of the same mantle velocity field makes it easier to analyze the effect of grain size variation on fluid migration.

To refer to FM models that employ the variable grain size fields from the T-GSE models, we use capital letters, A and B, corresponding to the T-GSE Models A and B, respectively. The prime symbol on the letters, A′ and B′, is used to indicate that the fluid influx occurs over an isolated depth range, and the double-prime symbol, A″ and B″, is used to indicate that the imposed influx pattern is calculated using a thermopetrologic model for the subducting slab (Table 3).

3. Results of Models With an Isolated Fluid Influx

3.1. Uniform Grain Size

We first consider cases with a uniform mantle wedge grain size of 1 mm and 1 cm, to provide clear descriptions of a scaling relationship between η and ϕ and critical fluid influx required for upward fluid migration and to illustrate the general fluid migration pattern that results from a uniform grain size distribution.

3.1.1. Scaling Relationship Between η and ϕ

For a given mantle velocity field and grain size distribution and with our assumption of constant fluid-mantle density difference, fluid velocity depends on ϕ^2/η (equations (2)–(4)). Thus, models with the same value of ${\phi_0}^2/\eta$ result in the same fluid migration pattern regardless of the specific values of η and ϕ. To illustrate this scaling relationship between η and ϕ, we present two simple FM models with a uniform grain size of 1 mm (FM Models I and II) (Figure 2). We assume an isolated fluid influx centered at y_0 of 100 km in both models. In Model I, $\bar{\phi}_0 = 0.01$ and $\eta = 1$ Pa s (Figures 2a–2c), and in Model II, $\bar{\phi}_0 = 0.001$ and $\eta = 0.01$ Pa s.

Table 3. FM Models With Variable Grain Size Shown in Figures

FM Model	Grain Size Distribution	Influx Pattern	Figure
A′	T-GSE A	y_0 = 75, 80, or 100 km	5
B′	T-GSE B	y_0 = 75, 80, or 100 km	5
A″	T-GSE A	Thermopetrologically consistent influx pattern	8
B″	T-GSE B	Thermopetrologically consistent influx pattern	8

These values are chosen arbitrarily, but in both models, the value of $\bar{\phi}_0{}^2/\eta$ is 0.0001. The resulting porosity field in the two models is different due to the difference in $\bar{\phi}_0$, but the fluid streamlines are identical, indicating that the exact values of η and ϕ are not important and that the value of $\bar{\phi}_0{}^2/\eta$ determines the fluid migration paths. Given the large uncertainties in the viscosity of aqueous fluids, we keep η constant at 1 Pa s in the remainder of the calculations and vary $\bar{\phi}_0$ to simulate a range of fluid migration paths for a given grain size distribution.

3.1.2. Effective Critical Fluid Influx for Upward Fluid Migration

For regions where the mantle flows downdip, such as at the base of the mantle wedge, it can be seen from equations (3) and (4) that when ∇P is negligibly small and thus $\vec{S}$ is upward, the ratio of the upward fluid flow rate to the downward mantle flow rate is

$$\frac{\phi^2 b^2 \Delta\rho g}{270\eta V_m \sin(\theta)} \tag{11}$$

There is a critical influx value (ϕ_c) that satisfies the above ratio of unity,

$$\phi_c = \left(\frac{270\eta V_m \sin(\theta)}{b^2 \Delta\rho g}\right)^{\frac{1}{2}} \tag{12}$$

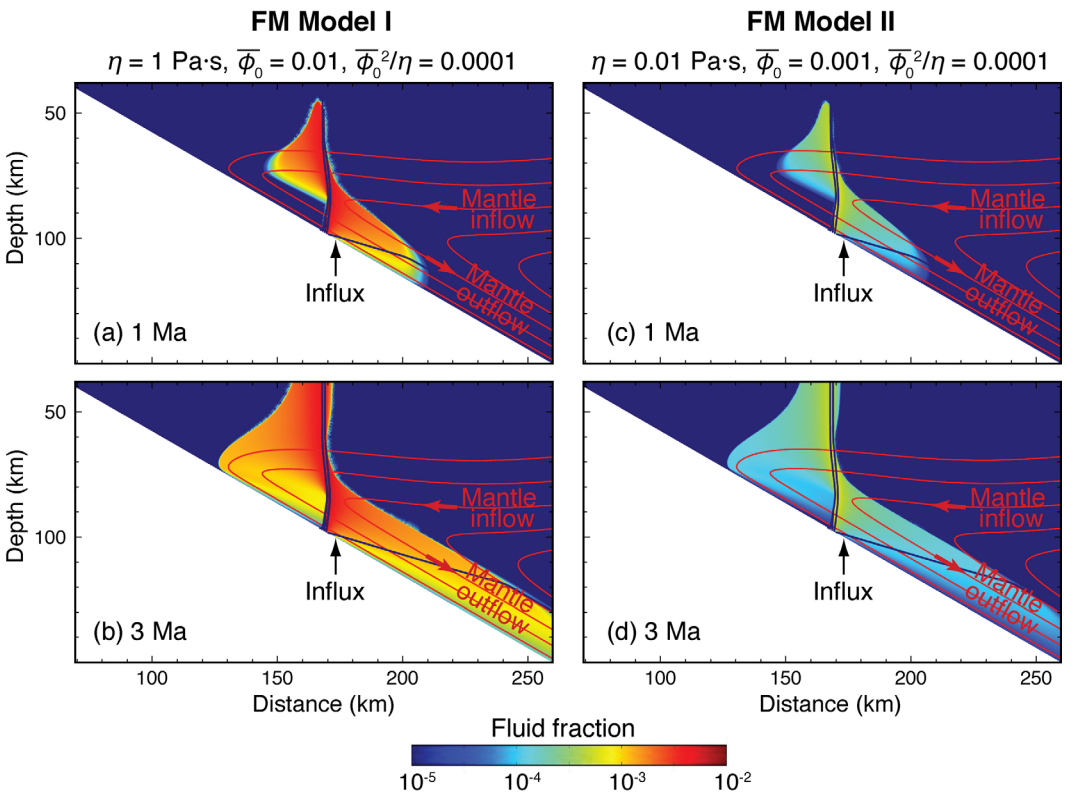

Figure 2. Fluid distribution (color) calculated by (a, b) FM Model I ($\bar{\phi}_0{}^2 = 0.01$ and $\eta = 1$ Pa s) and (c, d) FM Model II ($\bar{\phi}_0{}^2 = 0.001$ and $\eta = 0.01$ Pa s) at 1 and 3 Myr after the initiation of fluid influx with y_0 of 100 km, illustrating that fluid streamlines (dark blue lines) based on the fluid velocity field calculated at the given time step are identical for the same $\bar{\phi}_0{}^2/\eta$ value (0.0001). Only the fluid distribution is different between FM Models I and II. In this calculation, the mantle velocity field and the dynamic pressure distribution calculated by T-GSE Model A and uniform grain size of 1 mm are used. Red lines indicate mantle flow streamlines.

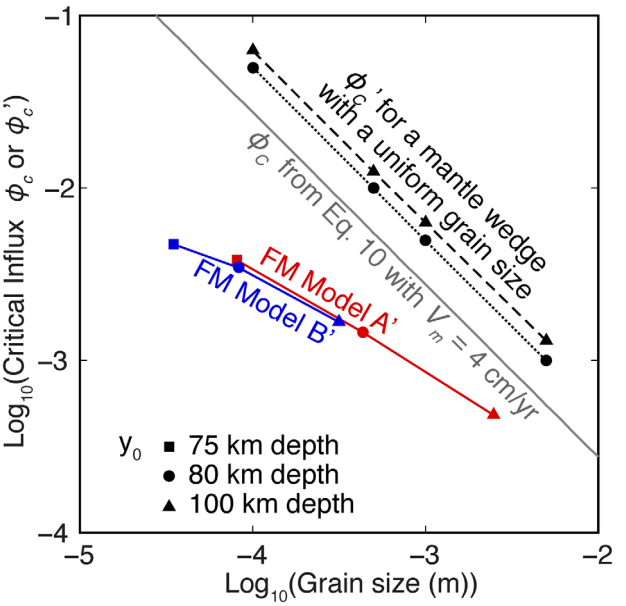

Figure 3. Effective critical influx values calculated for models with a uniform grain size (black) and FM Models A′ and B′ (red and blue, respectively). Grey dashed line indicates the critical influx value calculated from equation (12) with $V_m = 4$ cm/yr and $\theta = 30°$.

For $\phi = \phi_c$, fluid migration is horizontal. For $\phi < \phi_c$ and $\phi > \phi_c$, fluid migration is downdip and upward, respectively. We calculated critical influx values for a range of grain sizes using equation (12) assuming a constant V_m of 4 cm/yr and $\theta = 30°$ (grey line in Figure 3). As shown in equation (12) and Figure 3, ϕ_c is inversely related to the grain size *b*.

The above description of ϕ_c (equation (12)) with $V_m = 4$ cm/yr is applicable to the region immediately above the slab where the mantle flow velocity is comparable to the subduction rate and is relatively uniform, but it is not applicable to fluid migration in the inner part of the wedge where mantle velocity and grain size vary. To determine the minimal influx required to establish upward fluid migration paths within a given time scale (hereafter referred to as the effective critical influx ϕ_c'), we ran a series of simulations with different $\bar{\phi}_0$ values. For this exercise, we use the velocity field and the dynamic pressure distribution calculated by T-GSE Model A and impose an isolated fluid influx centered at either $y_0 = 80$ km (Figures 4a–4c) or 100 km (Figures 4d–4f).

We find that near the base of the mantle wedge, downdip fluid transport by mantle flow dominates over buoyancy-driven fluid migration. However, in the shallow part of the wedge where the mantle flows in from the back arc toward the trench, there are no mechanisms that drive the fluids downward. Therefore, if fluids reach the region of mantle inflow, an upward fluid migration path to the top of the wedge is eventually established. For this reason, ϕ_c' represents the minimum influx required for the fluids to reach the region of mantle inflow. We obtain values of ϕ_c' that permit fluids to reach the mantle inflow zone at 5 Myr after the initiation of fluid influx and present the fluid migration paths at 10 Myr after the fluid influx initiation to show the subsequent development of fluid migration paths (Figure 4). The purpose of employing a specific time scale in this study is to maintain consistency across different FM models. We note however that regardless of the choice of time scale, our modeling results provide quantitative descriptions for the evolution of fluid migration paths that can be interpreted across a range of geological time scales as a function of the imposed fluid influx. The relation between fluid influx and upward fluid velocity is discussed further in section 4.2.

For a uniform grain size of 1 mm and y_0 of 80 km (FM Model III), we find that if $\bar{\phi}_0 \leq 0.0049$, fluids become trapped in the downdip mantle flow and do not reach the surface (Figure 4a; Table 4). By contrast, if $\bar{\phi}_0 = 0.0050$, fluids reach the region of mantle inflow at 5 Myr after fluid influx initiation, resulting in eventual upward fluid migration (Figure 4b). Thus, for a grain size of 1 mm, $\phi_c' = 0.0050$. However, at ϕ_c', downdrag and upward fluid migration are nearly balanced, resulting in very slow upward migration, which does not reach the surface within the 10 Myr of our simulation (Figure 4b). Higher values of $\bar{\phi}_0$ above ϕ_c' result in more rapid development of vertical fluid migration pathways that reach the surface (e.g., Figure 4c). Similar results are obtained for y_0 of 100 km (FM Model IV; Figures 4d–4f).

For a given uniform grain size, our numerical results predict an inverse relation between ϕ_c' and *b* as observed for ϕ_c calculated from equation (12), but ϕ_c' is slightly greater than ϕ_c (black dots in Figure 3). The deviation of ϕ_c' from ϕ_c for a given grain size is attributed to the nonuniform distribution of ϕ_0 with depth, incorporation of dynamic pressure gradients, the nonuniform mantle flow velocity, and the effect of artificial diffusion. For a mantle wedge with a uniform grain size, the relation between ϕ_c' and grain size can be established from a few numerical simulations, and the general fluid migration path (upward or downward) is predictable.

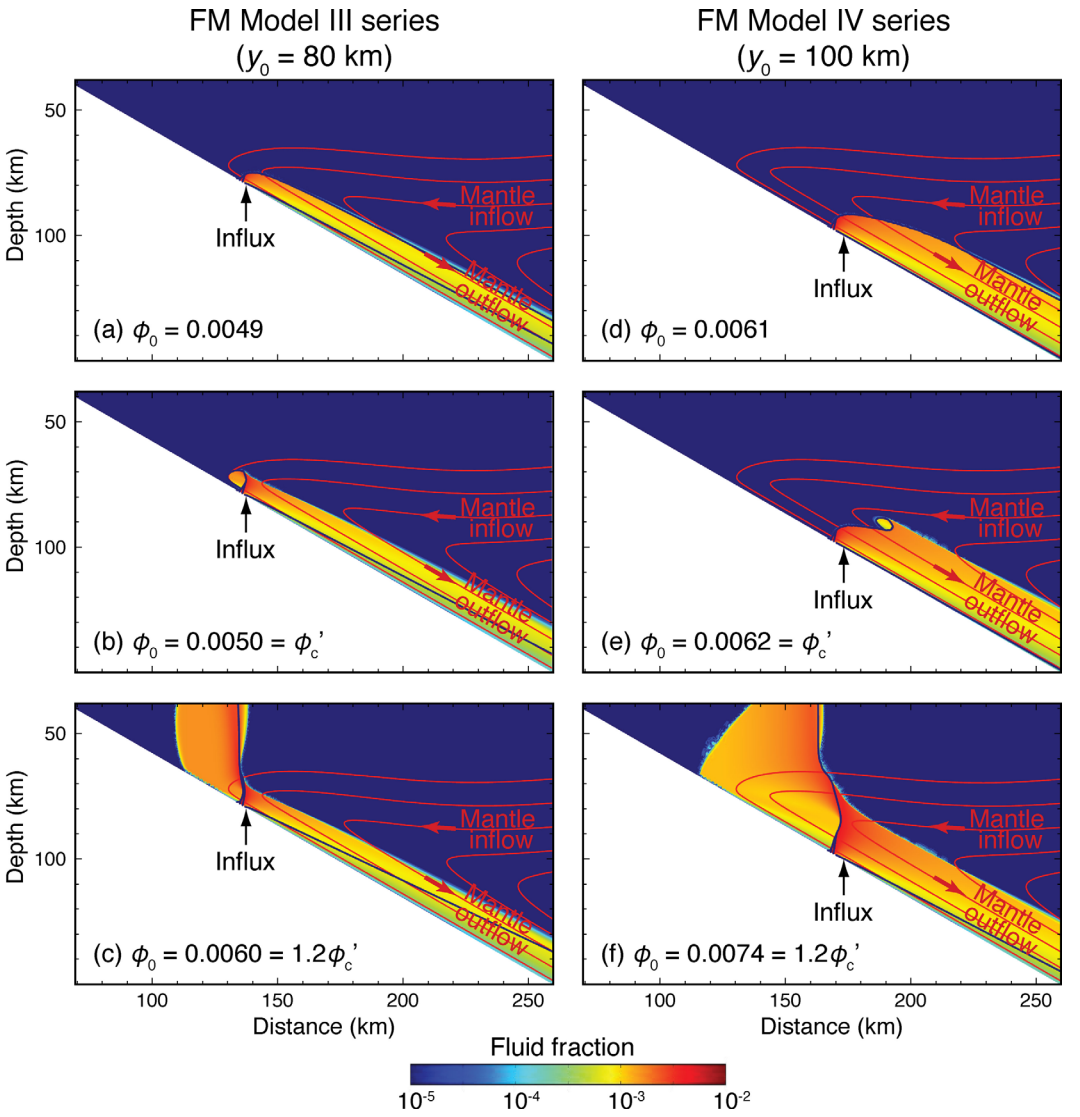

Figure 4. Fluid distribution (color) calculated by (a–c) FM Model III (y_0 = 80 km) and (d–f) FM Model IV (y_0 = 100 km) with a uniform grain size of 1 mm at 10 Myr after the initiation of fluid influx. The mantle velocity field and dynamic pressure distribution used in the models are calculated by T-GSE Model A. Red and dark blue lines indicate mantle and fluid streamlines, respectively. With influx below ϕ_c', all fluids travel downdip with the mantle. With influx at or above ϕ_c', some fluids migrate upward mostly trench-ward of the typical arc location beneath which the slab surface is situated at a depth of 80–120 km.

3.1.3. Fluid Migration Pattern

FM Models III and IV with $\bar{\phi}_0 \geq \phi_c$ (Figures 4b, 4c, 4e, and 4f) show that fluids introduced into the mantle wedge diverge into upward and downdip flow paths near the influx region. As discussed above, the upward migration is deflected toward the back arc near the base of the mantle wedge due to entrainment by the downdip mantle outflow. This is consistent with the flow pattern predicted by the model of *Cagnioncle et al.* [2007], in which a uniform and relatively large grain size is assumed. Our models also indicate that some of the fluids that travel upward into the region of mantle inflow become trapped in the inflowing mantle, move toward the wedge tip, and become recirculated back toward the influx region at an early stage of fluid migration. Only after this recirculation does upward fluid migration to the top of the mantle wedge become established.

The horizontal location of the predominant upward fluid pathway to the top of the mantle wedge depends on the fluid influx. When fluid influx is relatively low, such as the cases with $\bar{\phi}_0 = 1.2\ \phi_c$ (Figures 4c and 4f), the pathway develops trench-ward of the region of fluid influx due to transport by mantle inflow. With increasing fluid influx, the effect of mantle flow relaxes as permeability increases, and the pathway shifts away from the trench toward the region of fluid influx. FM Model I (Figures 2a and 2b) is equivalent to FM

Table 4. Effective Critical Influx (ϕ_c') for FM Models III and IV With a Uniform Grain Size of 1 mm (Figure 3)

	ϕ_c'	
b (mm)	FM Model III (y_0 = 80 km)	FM Model IV (y_0 = 100 km)
0.1	0.0496	0.0624
0.5	0.0099	0.0125
1	0.0050	0.0062
5	0.0010	0.0013

Model IV with $\bar{\phi}_0 = 0.01 \approx 1.6\ \phi_c$ and shows that with high fluid influx, a narrow pathway develops nearly directly above the region of fluid influx. The effect of melting, particularly in the region of mantle inflow, incorporated in the model of *Cagnioncle et al.* [2007] locally increases permeability, reducing the effect of trench-ward transport by the mantle inflow, and allowing the pathway to develop slightly toward the back arc relatively to the region of fluid influx. In our model, however, the upward fluid pathway does not shift toward the back arc beyond the influx region when the grain size in the mantle wedge is uniform.

3.2. Variable Grain Size

In the following models, we apply the grain size distributions calculated by T-GSE Models A and B to fluid migration models with an isolated fluid influx (FM Models A′ and B′, respectively). For FM Models A′ and B′, we investigate y_0 = 75, 80, or 100 km. The grain size at the base of the mantle wedge at y_0 for each model is summarized in Table 1. As in section 3.1.2, we obtain ϕ_c' that permits fluids to reach the region of mantle inflow at 5 Myr after fluid influx initiation. The fluid migration occurs more slowly in these models than those in section 3.1.2 due to presence of very small grain sizes (<1 mm) at the base of the mantle wedge (Figure 1b), and we present the fluid migration paths at 20 Myr after fluid influx initiation to show the subsequent development of fluid migration paths (Figure 5). The resulting ϕ_c' values for FM Models A′ and B′ with different influx depths are summarized in Table 5.

In FM Model A′ (V_m = 4 m/yr, slab age = 10 Ma), fluids introduced at y_0 = 75 km tend to remain near the base of the mantle wedge at shallow depths (Figure 5a). Note that the porosity immediately above y_0 is caused by recirculation of fluid that has risen above the region of downdip mantle outflow and is entrained in the mantle inflow. This fluid migration pattern contrasts with the uniform grain size models, in which predominant upward migration pathway starts to develop immediately above the influx region (Figure 4). The downdip drag in FM Model A′ occurs because the mantle at the base of the mantle wedge is less permeable due to its fine grain size, entraining the fluids. However, as fluids move downdip, grain size increases (as the mantle warms) and permeability increases, resulting in eventual upward fluid migration. With increasing y_0, the initial down-drag becomes less prominent because the grain size where the fluid is introduced is greater, resulting in higher permeability that allows faster initiation of upward fluid migration. A corollary to this is that in simulations with variable grain size, ϕ_c' decreases with increasing y_0 (Table 5; Figure 3) because grain size, and thus permeability, increases with y_0, requiring smaller influx to cause upward fluid migration. Further, ϕ_c' at a given influx depth is greater for a colder slab because of the smaller grain size and lower permeability (Table 1; Figure 1b).

Using the grain size at y_0 (Table 1), we plot ϕ_c' determined for FM Models A′ and B′ against grain size b in Figure 3. It shows that ϕ_c' has an inverse relation with b, similar to those in models with a uniform grain size (FM Models III and IV). Unlike in the uniform grain size case, the relation between ϕ_c' and b in FM Models A′ and B′ cannot be described by a single mathematical expression given the spatial variation in b. However, the results provide a general sense of the effect of grain size variation; ϕ_c' is smaller and less dependent on b (at a given y_0) in FM Models A′ and B′ than in models with a uniform grain size. This can likely be attributed to the increase in grain size in both the downdip and upward directions in FM Models A′ and B′. (Based on least squares regression, ϕ_c' is proportional to $b^{-0.55}$.)

Despite the difference in the grain size distribution between FM Models A′ and B′, the critical influx values are comparable for a given grain size at the influx region (Figure 3). Near the base of the mantle wedge, grain size is predicted to increase gradually with depth in most subduction settings (Figure 1c), and the overall pattern of grain size does not change significantly among different subduction settings [*Wada et al.*, 2011]. Given the robust grain size distribution in the mantle wedge, the critical fluid influx is relatively invariant for influx regions with similar grain size.

4. Results of Models With a Thermopetrologically Consistent Fluid Influx Distribution

Next, we apply a more realistic fluid influx distribution to the fluid migration model. We first calculate the pattern of H_2O release from the subducting slab, using the slab thermal structure calculated by T-GSE

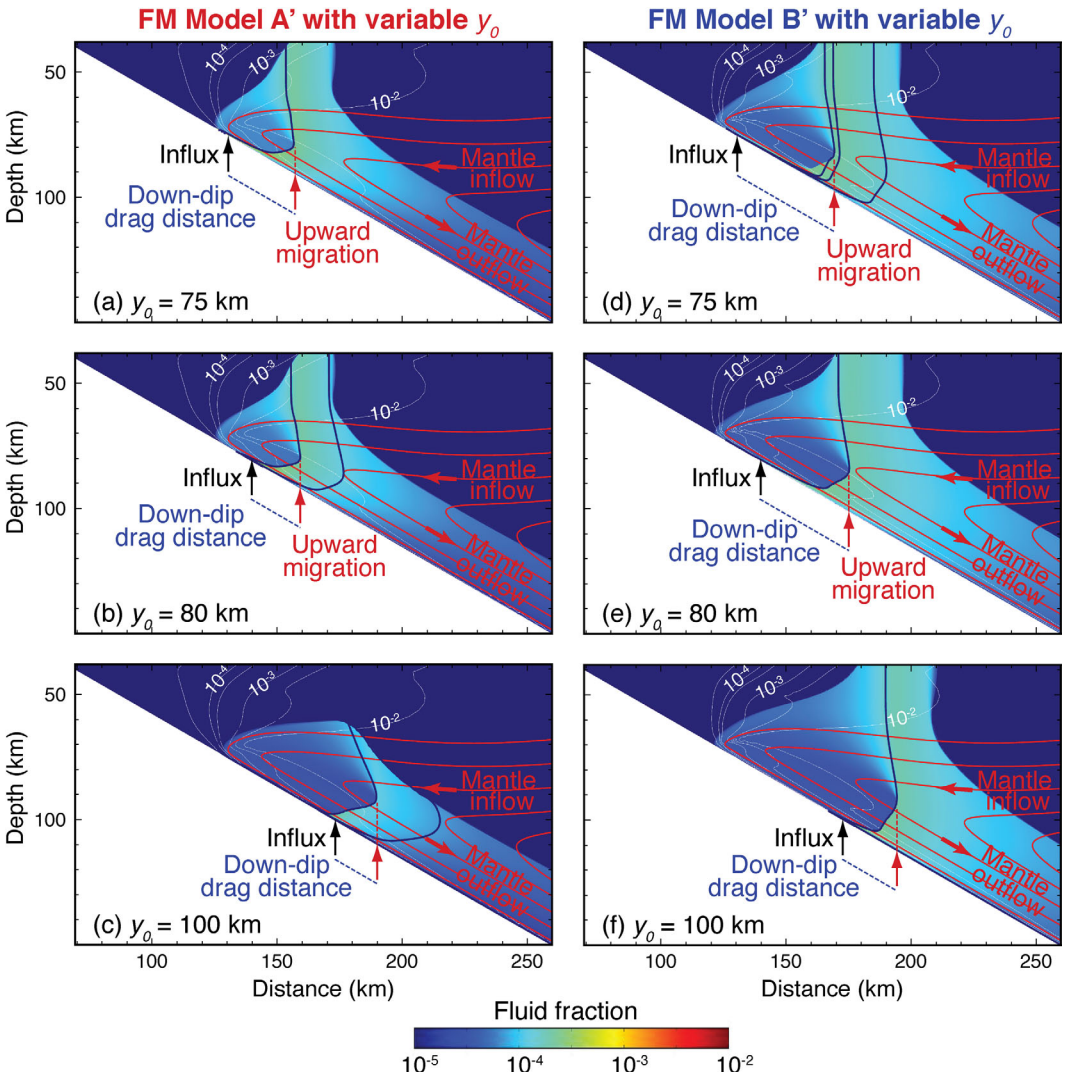

Figure 5. Fluid distribution (color) calculated by (a–c) FM Model A′ and (d–f) FM Model B′ at 20 Myr after the initiation of fluid influx at its critical value. The grain size distribution, mantle flow field, and dynamic pressure distribution applied to A′ and B′ are calculated by T-GSE Models A and B, respectively. (a, d) y_0 = 75 km, (b, e) y_0 = 80 km, and (c, f) y_0 = 100 km. The effective critical influx values ϕ_c' are (a) 0.0038, (b) 0.0015, (c) 0.0005, (d) 0.0047, (e) 0.0034, and (f) 0.0017. Thin white contours indicate grain size (m). Red and dark blue lines indicate mantle and fluid streamlines, respectively.

Models A and B and the thermodynamic calculation code Perple_X [*Connolly*, 2009]. The calculation is carried out following the approach of *Wada et al.* [2012]. In the calculation, we adopt a generic lithologic model of *Hacker* [2008] for the oceanic slab, in which the top 11 km of the slab is assumed to be hydrated and consists of a 0.3 km-thick upper volcanic layer, a 0.3 km-thick lower volcanic layer, 1.4 km-thick dikes, 5 km-thick gabbros, and 4 km-thick upper mantle, with initial bulk H_2O contents of 3.1, 2.6, 1.8, 0.8, and 2.0 wt %, respectively. The mass of H_2O released from the 11 km-thick column normalized to a unit surface area at a given depth is shown in Figure 6a, and the cumulative mass of H_2O released from the slab is shown in Figure 6b. The relatively warm slab thermal structure in T-GSE Model A results in shallow dehydration, and the slab releases nearly all its minerologically bound H_2O in the crust and the mantle before it reaches a depth of 103 km, with peak dehydration between 67 and 103 km depth. By contrast, the slab in Model B is colder and retains H_2O in the lower crust and upper mantle to

Table 5. Effective Critical Influx (ϕ_c') for FM Models A′ and B′ at a Given Influx Depth (y_0)

	ϕ_c' With a Given y_0		
FM Model	75 km	80 km	100 km
A′	0.0038	0.0015	0.0005
B′	0.0047	0.0035	0.0017

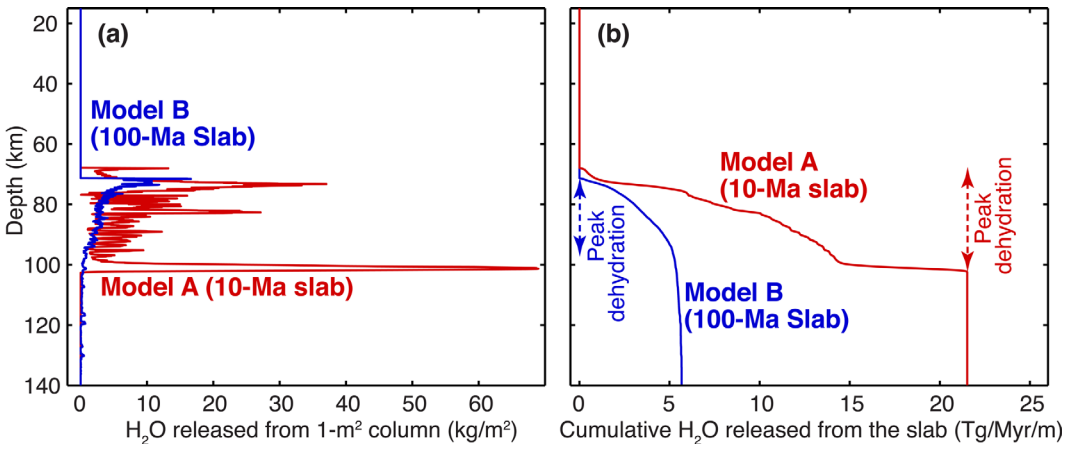

Figure 6. (a) Total amount of H_2O released from a unit vertical column (kg/m^2) of the 11 km-thick hydrated section of the slab. (b) Cumulative amount of H_2O (Tg/Myr/m) released from the slab. In both Figures 6a and 6b, the vertical axis indicates the surface depth of the column. Red and blue dashed lines with arrowheads in Figure 6b indicate the depth range of peak dehydration for Models A and B, respectively.

greater depths; fluids released at 72–97 km depths are derived largely from the dehydration of the upper crust.

At the pressures and temperatures appropriate for the mantle wedge, the density of H_2O is approximately 1000 kg/m^3 [*Zhang and Duan*, 2005]. Although fluids at mantle wedge temperatures are likely to be silica-rich and also may contain siliceous melts, for simplicity we neglect the compositional effects on fluid density and use 1000 kg/m^3 to convert the calculated mass of H_2O released from 1 m^2 column to volumetric H_2O (see section 5.2 for discussion on the potential effects of this assumption on our modeling results). We then calculate the volumetric flux using the subduction rate assumed in the T-GSE model. This volumetric flux does not necessarily correspond to the influx rate at the base of the mantle wedge. One reason is that the rate assumes the instantaneous migration of all H_2O released from different parts of a given slab column to the surface. In reality, it takes some time for released H_2O to migrate through the slab and some H_2O may not reach the slab surface—thus the actual influx rate is likely lower. Another reason is that the influx into the mantle wedge depends on the permeability contrast between the wedge and the underlying material [*Wilson et al*., 2014]. We do not parameterize the time scale of H_2O migration in the slab or the permeability contrast. Instead, we simply scale the calculated volumetric flux such that fluids reach the region of mantle inflow at 5 Myr after fluid influx initiation. The influx scaling factor ω that meets the criteria is determined through trial and error. The scaled depth-dependent fluid influx ($Q_f(y)$) is converted to fluid fraction at the base of the mantle wedge:

$$\phi_0(y) = \left(-\frac{270\eta Q_f(y)\omega}{b^2 \Delta\rho g} \right)^{-\frac{1}{3}} \tag{13}$$

4.1. Uniform Grain Size

Figure 7 shows the fluid migration paths in the mantle wedge for a uniform grain size of 1 mm (FM Model V) and 10 mm (FM Model VI) that result from the application of the depth-dependent fluid influx calculated by T-GSE Model A. The values of ω (equation (13)) used in the two models are 5.9×10^{-2} and 0.6×10^{-2}, respectively. In both cases, fluids introduced at $<\sim$95 km depths are initially dragged downdip by the downgoing mantle flow because both grain size and fluid influx at these depths are relatively small, and permeability is not large enough to allow upward fluid migration (Figures 7a and 7b). However, at $\sim$100 km depth, a large pulse of fluid influx from the warm slab in T-GSE Model A (Figure 6a) combined with the migration of fluids from the shallow depths causes the initiation of upward fluid migration. Fluids then start to migrate upward while being strongly deflected back toward the trench due to the effect of mantle inflow. A dominant upward fluid migration pathway is eventually established significantly trench-ward from the observed location of most arcs, beneath which the slab surface is situated at a depth of 80–120 km depth. An increase in the magnitude of fluid influx will result in faster upward fluid migration, and the

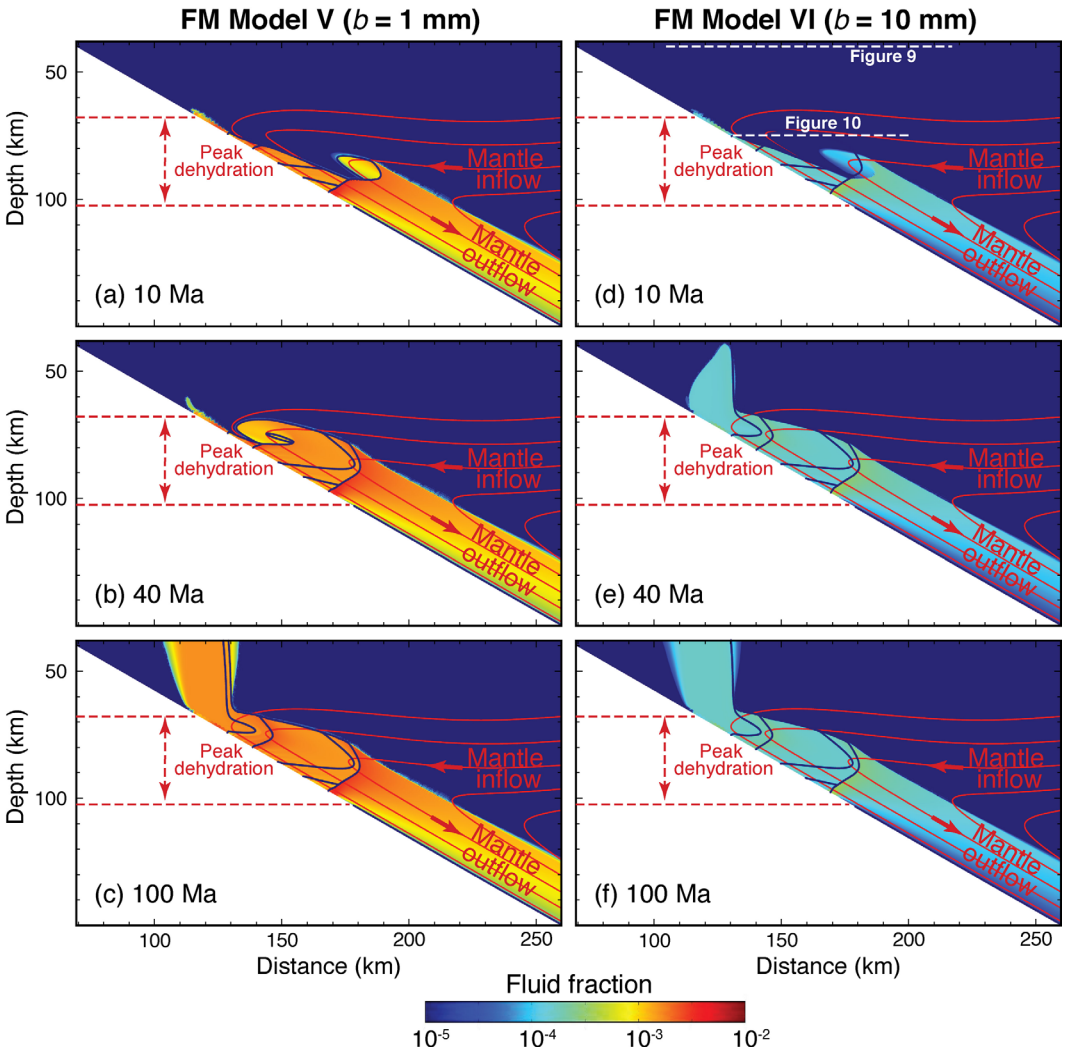

Figure 7. Fluid distribution (color) calculated by FM Model V with an influx distribution calculated for T-GSE Model A and a uniform grain size of (a–c) 1 mm and (d–f) 10 mm at 10, 40, and 100 Myr after the initiation of fluid influx. Influx scaling factors of 5.9×10^{-2} and 0.6×10^{-2}, respectively, are used. The mantle velocity field and dynamic pressure distribution used in the models are also calculated by T-GSE Model A. Red and dark blue lines indicate mantle and fluid streamlines, respectively. White dashes lines in Figures 7a and 7d indicate the location of profiles used in Figures 9 and 10.

formation of a dominant upward fluid migration pathway directly above the influx region. However, this pathway does not shift toward the back arc beyond the region of fluid influx (corresponding to slab depths of 70–100 km) when the grain size is uniform, as discussed in section 3.1.3.

4.2. Variable Grain Size

We next applied the depth-dependent fluid influx with the grain size distributions calculated by T-GSE Models A and B; the resulting fluid migration models are referred to as FM Models A″ and B″ (Figure 8). The influx scaling factors used in the two models are 8.9×10^{-5} and 6.8×10^{-6}, respectively. Despite the wider region of fluid influx, the fluid migration pattern in these runs is similar to the cases in section 3.2 with isolated fluid influx. Fluids in FM Models A″ and B″ are initially dragged downdip along the base of the mantle wedge by mantle flow due to fine grain size (Figures 8a and 8f), and the downdip drag distance is longer in Model B″ than in Model A″′ due to finer grain size. As fluids travel downdip, grain size increases, allowing upward fluid migration and development of a predominant pathway that focuses fluids into a relatively narrow region beneath the arc (fluid flow streamlines in Figure 8). The predominant pathway near the top of the mantle wedge (at ~40 km depth) appears where the slab reaches a depth of 102 km in FM Model A″ and 109 km in FM Model B″ at ~20 Myr after fluid influx initiation (Figure 9). During the next 10 Myr, the

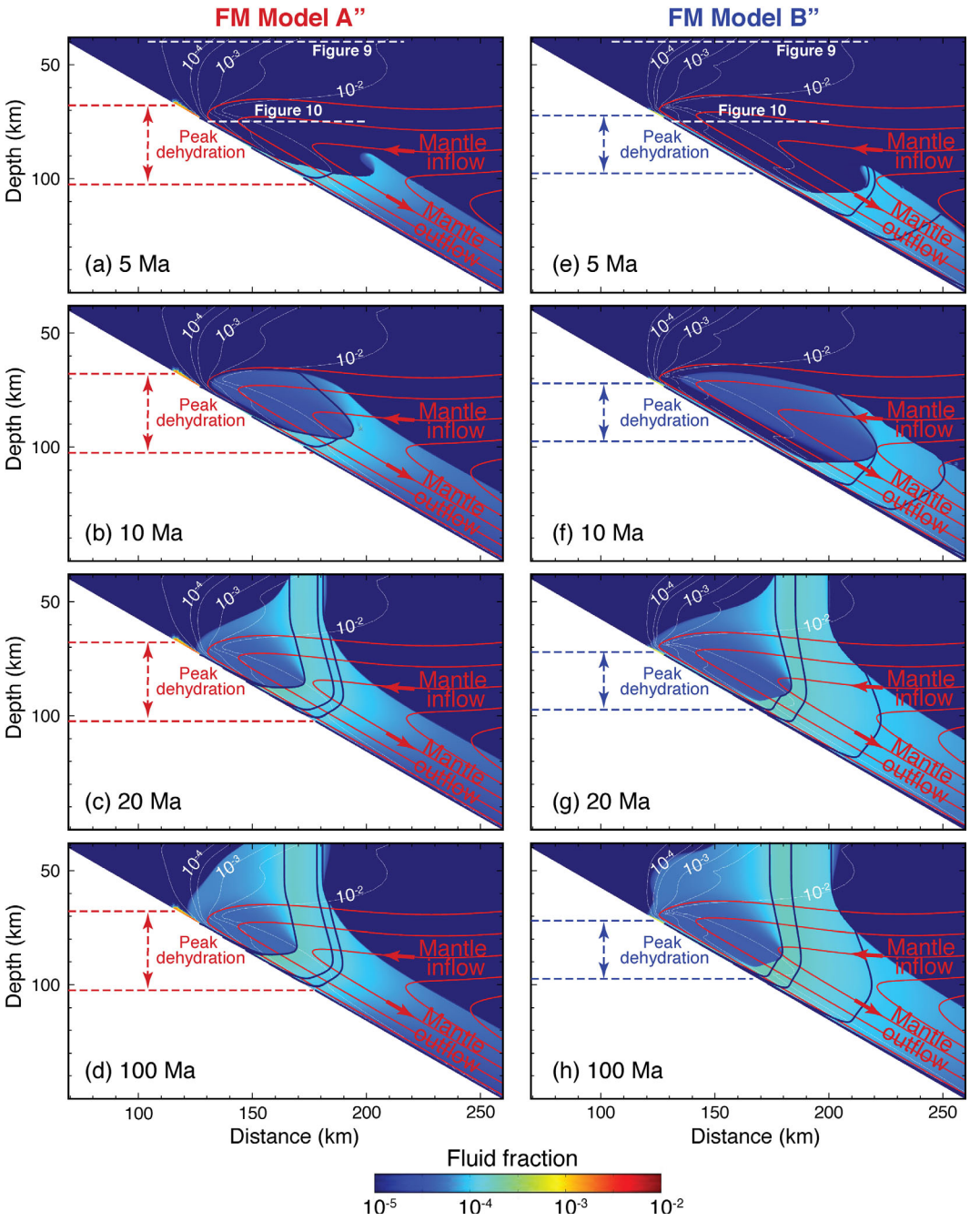

Figure 8. Fluid distributions (color) predicted by (a–d) FM Model A″ and (e–h) FM Model B″ at 5, 10, 20, and 100 Myr after fluid influx initiation. The influx distribution is based on the patterns of H_2O release calculated for a 10 Ma slab and a 100 Ma slab, respectively. Influx scaling factors of 8.9×10^{-5} and 6.8×10^{-6}, respectively, are used. The grain size distribution, mantle flow field, and dynamic pressure distribution applied to A″ and B″ are calculated by T-GSE Models A and B, respectively. Red and blue horizontal dashed lines indicate the depth range of peak dehydration (Figure 7b) for FM Models A″ and B″, respectively. White dashes lines in Figures 8a and 8e indicate the location of profiles used in Figures 9 and 10. Red and dark blue lines indicate mantle and fluid streamlines, respectively.

horizontal location shifts slightly toward the trench and then reaches steady state, at which the predominant pathway is situated where the slab reaches a 100 km depth in FM Model A″ and a 106 km depth in FM Model B″, in good agreement with the observed average location of the arc [*England et al.*, 2004; *Syracuse and Abers*, 2006]. This is in strong contrast with Model V with a uniform grain size (Figure 7).

The rates of upward fluid migration in Models A″ and B″ are comparable because fluid influx is scaled. The peak upward fluid velocity at a 75 km depth at 20 Myr after fluid influx initiation is 14 and 16 cm/yr,

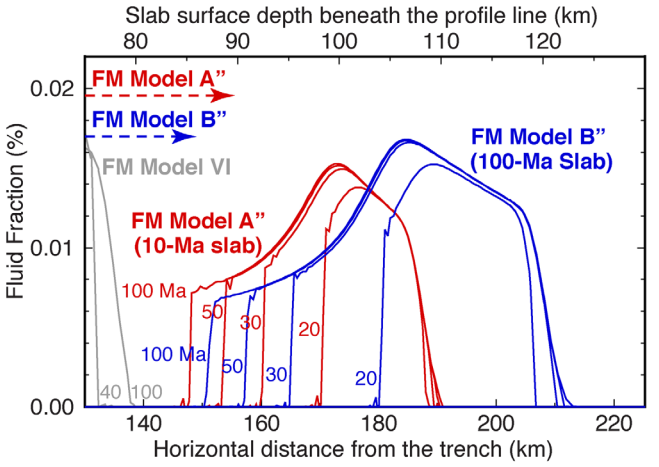

Figure 9. Change in fluid fraction with time along a horizontal profile line at a depth of 40 km as shown in Figures 7a and 7d and 8a and 8f. Red and blue lines indicate FM Models A″ and B″, respectively. The horizontal locations of the peak fluid fraction in the shallow part of the mantle wedge in FM Models A″ and B″ are comparable to that of the typical arc location. Dashed lines with an arrowhead indicate the down-dip extent of peak dehydration depth calculated for FM Models A″ and B″ (Figure 6). In all three models, fluid fraction along the 40 km depth profile line at 10 Ma is zero because fluids have not reached the 40 km depth.

respectively (Figure 10). The peak upward fluid velocity increases slightly with time, reaching steady state at 40 Myr at 16 cm/yr and 19 cm/yr, respectively. In this study, we chose an influx scaling factor such that upward fluid migration initiated at 5 Myr after flux initiation for consistency. Using a shorter time scale, for example, simply requires a larger influx scaling factor, which results in higher peak vertical fluid velocities. We discuss the relevance of the time scale used in our model to the geochemical inferences for the time scale of upward fluid migration in section 5.2.

The values of the scaling factors used for the above two models indicate that much less H_2O is required in Model B″ than in Model A″ to cause fluids to reach the region of mantle inflow in a given time scale. As will be discussed in section 5.3, the smaller influx in Model B″ may be consistent with what happens in a real subduction system, in which greater permeability contrast between the base of the mantle wedge and the underlying material is likely to exist due to finer grain size at the base of the mantle wedge in Model B″ than in Model A″, resulting in less fluid influx.

5. Discussion

5.1. Uniform Location of the Arc

Given that the temperature in the mantle wedge is high enough to induce hydrous melting over a wide region, the distribution of aqueous fluids that trigger hydrous melting is a likely key factor that controls the location of the volcanic arc. However, aqueous fluids are released from a slab at various depths [*Hacker*, 2008; *van Keken et al*., 2011] (Figure 6), and fluid influx into the mantle wedge over a wide depth range is expected. Thus, there appears to be a mechanism that regulates the location of hydrous melting and arc volcanoes, which tend to form above the point at which the slab reaches a depth of 80–120 km as discussed in section 1.

The effect of mantle outflow can cause some downdip fluid migration, but the travel distance is relatively small before fluids start to migrate upward (Figures 4 and 7) [*Cagnioncle et al*., 2007]. Hydrous phases in the mantle wedge can also provide a downdip transport mechanism [*Iwamori*, 1998, 2007; *Hebert et al*., 2009], but our T-GSE model as well as other thermal models that adopt temperature-dependent mantle rheology and a slab-mantle coupling depth of 70–80 km indicate relatively high temperatures that make it difficult for a volumetrically significant amount of hydrous phases to form at the base of the mantle wedge at depths >80 km [*van Keken et al*., 2011; *Wada et al*., 2012].

Our modeling results indicate that the grain size distribution in the mantle wedge can provide a possible mechanism for focusing of upward fluid migration at a relatively uniform location with respect to the slab surface. Fine grain sizes immediately above the slab at the base of the mantle wedge enhance the initial downdip transport of fluids. However, as the thermal and deformation conditions above the slab evolve, the corresponding downdip increase in grain size promotes upward fluid migration where the slab reaches a depth of ~100 km, within the typical subarc slab depth range (Figures 8 and 9). Further, fluids released in the back arc rise upward into the top half of the mantle wedge and eventually start to migrate back toward the trench due to the influence of mantle inflow and the buoyancy. The combination of downdip fluid transport just above the slab and trench-ward migration of fluids in the upper half of the mantle wedge

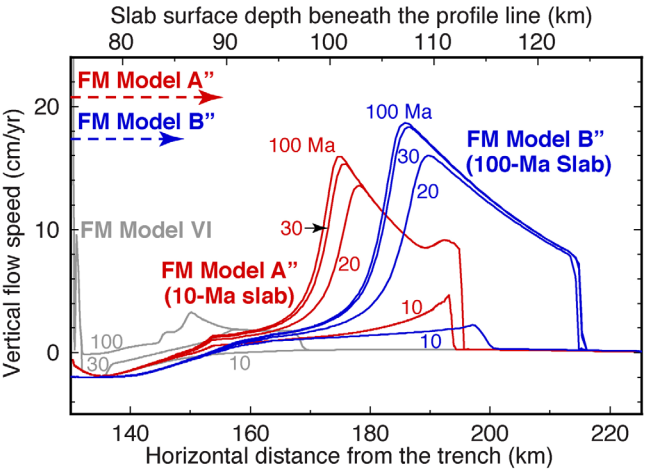

Figure 10. Change in vertical speed of fluid flow with time along a horizontal profile line at a depth of 75 km as shown in Figures 7a and 7d and 8a and 8f. Red and blue lines indicate FM Models A″ and B″, respectively. Positive velocity values indicate upward fluid migration. Upward fluid velocities in the central part of the mantle wedge (e.g., 75 km depth as shown) in FM Models A″ and B″ evolve to values that are comparable to those inferred from U series disequilibria in arc lavas. Vertical fluid velocities in all three models change little after ~40 Ma.

tends to result in the development of a predominant upward fluid migration pathway focused where the slab reaches a depth of 80–120 km. This provides steady fluid supply at a relatively uniform location for hydrous melting and arc volcanism.

Lateral migration of fluids in the mantle wedge may also result from the effect of compaction pressure [*Wilson et al.*, 2014], which is neglected in our model. The fluid migration model of *Wilson et al.* [2014] indicates that if fluids have high mobility relative to the moving mantle, fluids released from the subducting slab in the back-arc region tend to migrate updip within the slab for some distance before rising upward into the mantle wedge, focusing fluids beneath the arc region. This may also be an important mechanism that prevents wide spread volcanism in the back-arc region. Future modeling studies that include both mantle grain size variations and compaction pressure are required to unravel the relative importance of these two effects on fluid migration in the mantle wedge.

5.2. Time Scale for Establishing Fluid Pathway and Fluid Migration

In this study, we simulated fluid migration such that upward fluid migration is initiated at 5 Myr after fluid influx initiation and present the subsequent evolution of fluid migration paths. In FM Models A″ and B″ with grain size variations and a realistic fluid influx pattern (Figure 8), fluids then reach the top of the mantle wedge 15–20 Myr after the initiation of fluid influx. This represents the time required to establish fluid migration pathways that traverse the entire mantle wedge based on the time scale that we have chosen. Once the stable migration pathways are established, fluids migrate at a relatively fast rate of 15–20 cm/yr through the pathways (Figure 10).

The time scale used in our study was chosen to illustrate the effects of grain size variation on fluid migration, but ideally, it should be chosen based on geologic parameters and result in a realistic timeframe that reflects the occurrence of arc volcanism following subduction initiation. However, the time scale for the establishment of fluid migration pathways is difficult to constrain.

One useful clue is the travel time of melts inferred from U series disequilibria in arc lavas. Fluid addition and partial melting in the mantle wedge can disturb secular equilibrium of U series isotope ratios, such as $^{230}Th/^{238}U$, $^{226}Ra/^{230}Th$, and $^{231}Pa/^{235}U$, and their disequilibria therefore provide constraints on the timing of fluid addition and partial melting in the mantle wedge—although it is difficult to distinguish the contributions of the two processes to the disequilibria and to reconcile disequilibria of different isotope ratios from a given arc lava [*Peate and Hawkesworth*, 2005, references therein]. Accordingly, there are wide estimates on travel time of melts based on the disequilibrium data, ranging from a few thousand to a few hundred thousand years [*Turner et al.*, 2000; *Bourdon et al.*, 2003; *Peate and Hawkesworth*, 2005], which generally indicate relatively fast melt migration. Although the applicability of the time scale chosen in our study requires further investigation, the ascent speeds calculated by our models result in a few hundred thousand years of migration time from a melt source region to the surface after an efficient vertical conduit is established.

In our model, the effect of melt generation is not included. Silicate melts are denser and less buoyant than silica-rich aqueous fluids. However, the effect of higher fluid fraction upon melting causes higher permeability and faster fluid migration (equation (3)). Thus, once melting occurs, the upward fluid velocities may

increase despite the increase in density. Further, faster fluid migration at shallower depths in the lithosphere is expected due to fluid migration through network of fractures. Thus, the upward fluid velocity at 40 km depth may be underestimated by our model.

Reubi et al. [2014] suggest that the time lag between mantle metasomatism and melting inferred from U series disequilibria can vary from a few hundred years to >350 kyr among different subduction zones. Their geochemical model assumes that metasomatized mantle travels upward from the base of the mantle wedge to the region of high temperature for melt generation, explaining the relatively long time lag between mantle metasomatism and melting. This mode of water transport is different from our model, in which we assume that the mantle follows the corner flow pattern and water migrates as a free fluid into the melting region. The migration of metasomatized mantle to the melt region may be another important mechanism for water transport in the mantle wedge.

5.3. Factors Regulating Fluid Influx and Melt Generation

Although fluid influx is imposed in our model, the actual amount of fluid influx in a real subduction system depends on the permeability of the mantle at the base of the wedge relative to the underlying slab material. The T-GSE model predicts smaller grain size for subduction zones with colder slabs, and the difference in grain size at a given depth can be as much as 1 order of magnitude between the warm and cold-slab cases (Figure 1c). Thus, permeability of the mantle above a cold slab can be 2 orders of magnitude lower than that above a warm slab. If we assume that the permeability of the slab at a given depth does not vary much among different subduction zones, the permeability contrast with respect to the underlying slab is 2 orders of magnitude greater in cold-slab subduction zones. Further, if the permeability of older slabs is greater than younger slabs because, for example, older plates are subjected to deformation (faulting and fracturing) over a longer period of time prior to subduction, then it also contributes to increasing the permeability contrast in cold-slab subduction zones. Larger permeability contrast in colder-slab subduction zones would result in a smaller fraction of aqueous fluids that migrate into the mantle wedge. Although our model does not include the subducting slab, the results imply that compared to warmer slab subduction zones much less fluid influx is required in colder-slab subduction zones to cause comparable upward fluid migration rates, consistent with the trend that would result from larger permeability contrast in colder-slab subduction zones. Fluids that do not migrate into the mantle wedge are likely to travel updip through the subducting material and may eventually migrate into the mantle wedge at shallower depths if the permeability of the overlying mantle wedge is comparable to that of the underlying subducting material or dynamic pressure gradients drive such migration [*Wilson et al*., 2014]. The investigation of the role of permeability contrast and dynamic pressure gradients across the slab-mantle boundary in regulating fluid influx and melt generation is an area of future studies.

6. Summary

We have developed a fluid migration model that incorporates the effects of grain size variations in the mantle wedge. Our results indicate that fluids introduced into the mantle wedge beneath the fore-arc region are dragged downdip by mantle flow due to small grain size and low permeability near the base of the mantle wedge. As grain size increases with depth, permeability increases, resulting in the development of upward fluid migration paths. Similarly, fluids released in the back arc are also initially dragged downdip by the downgoing mantle, and the ultimate fate of these fluids is controlled by the relative permeability of the mantle wedge and the downgoing mantle velocity, with some fluids continuing to travel downdip and others migrating upward where they are eventually transported back toward the trench with the inflowing mantle. The downdip transport of fluids beneath the fore arc and opposite trench-ward transport of rising fluids beneath the back arc result in a focusing of upward fluid migration. The horizontal location of the predominant fluid pathway is relatively insensitive to the slab thermal structure despite its effect on the depths of fluid influx and is located where the slab reaches a depth of ~100 km, similar to the position of the arc in natural subduction zones. This pattern of fluid migration contrasts with those in models with uniform grain size, in which an upward fluid migration pathway develops in the fore-arc region away from the arc. Grain

size variation in the mantle wedge therefore is an important factor that controls upward fluid migration in the mantle wedge and thus the location of the volcanic arc in subduction zones.

Acknowledgments
We thank E.M. Parmentier, C.R. Wilson, and M. Spiegelman for helpful discussions on modeling approaches at an earlier stage of this work and L.G.J. Montési and two anonymous reviewers for their thorough review, which helped to improve our manuscript. This work was supported by Intramural Research Grant for Special Research Projects from the International Research Institute of Disaster Science, Tohoku University, Japan (IW) and NSF sward EAR-1316333 (M.D.B.). Preparatory work for this project was supported by a MARGINS Postdoctoral Fellowship to I.W. (NSF OCE-0840800). The data plotted in all figures and the codes used for T-GSE models and fluid flux calculations can be accessed by contacting IW.

References

Austin, N. J., and B. Evans (2007), Paleowattmeters: A scaling relation for dynamically recrystallized grain size, *Geology*, *35*, 343–346.
Behn, M. D., G. Hirth, and J. R. Elsenbeck II (2009), Implications of grain size evolution on the seismic structure of the oceanic upper mantle, *Earth Planet. Sci. Lett.*, *282*, 178–189.
Bourdon, B., S. Turner, and A. Dosseto (2003), Dehydration and partial melting in subduction zones: Constraints from U-series disequilibria, *J. Geophys. Res.*, *108*(B6), 2291, doi:10.1029/2002JB001839.
Cagnioncle, A.-M., E. M. Parmentier, and L. Elkins-Tanton (2007), Effect of solid flow above a subducting slab on water distribution and melting at convergent plate boundaries, *J. Geophys. Res.*, *112*, B09402, doi:10.1029/2007/JB004934.
Connolly, J. (2009), The geodynamic equation of state: What and how, *Geochem. Geophys. Geosyst.*, *10*, Q10014, doi:10.1029/2009GC002540.
Currie, C. A., K. Wang, R. D. Hyndman, and J. He (2004), The thermal effects of steady-state slab-driven mantle flow above a subducting plate: The Cascadia subduction zone and back arc, *Earth Planet. Sci. Lett.*, *223*, 35–48.
Davies, J. H., and D. J. Stevenson (1992), Physical models of source region of subduction zone volcanic, *J. Geophys. Res.*, *97*, 2037–2070.
England, P. C., and R. F. Katz (2010), Melting above the anhydrous solidus controls the location of volcanic arcs, *Nature*, *467*(7316), 700–703.
England, P. C., R. Engdahl, and W. Thatcher (2004), Systematic variation in the depths of slabs beneath arc volcanoes, *Geophys. J. Int.*, *156*, 377–408.
Evans, B., J. Renner, and G. Hirth (2001), A few remarks on the kinetics of static grain growth in rocks, *Int. J. Earth Sci.*, *90*, 88–103, doi:10.1007/s005310000150.
Furukawa, Y. (1993), Depth of the decoupling plate interface and thermal structure under arcs, *J. Geophys. Res.*, *98*, 20,005–20,013.
Gaetani, G. A., and T. L. Grove (1998), The influence of water on melting of mantle peridotite, *Contrib. Mineral. Petrol.*, *131*, 323–346.
Grove, T., C. Till, E. Lev, N. Chatterjee, and E. Médard (2009), Kinematic variables and water transport control the formation and location of arc volcanoes, *Nature*, *459*(7247), 694–697, doi:10.1038/nature08044.
Grove, T. L., N. Chatterjee, S. W. Parman, and E. Medard (2006), The influence of H_2O on mantle wedge melting, *Earth Planet. Sci. Lett.*, *249*, 74–89.
Hacker, B. R. (2008), H_2O subduction beyond arcs, *Geochem. Geophys. Geosyst.*, *9*, Q03001, doi:10.1029/2007GC001707.
Hacker, B. R., G. A. Abers, and S. M. Peacock (2003), Subduction factory: 1. Theoretical mineralogy, densities, seismic wave speeds, and H_2O contents, *J. Geophys. Res.*, *108*(B1), 2029, doi:10.1029/2001JB001127.
Hall, C. E., and E. M. Parmentier (2003), Influence of grain size evolution on convective instability, *Geochem. Geophys. Geosys.*, *4*(3).
Hebert, L. B., and L. G. J. Montési (2013), Hydration adjacent to a deeply subducting slab: The roles of nominally anhydrous minerals and migrating fluids, *J. Geophys. Res. Solid Earth*, *118*, 5753–5770, doi:10.1002/2013JB010497.
Hebert, L. B., P. Antoshechkina, P. Asimow, and M. Gurnis (2009), Emergence of a low-viscosity channel in subduction zones through the coupling of mantle flow and thermodynamics, *Earth Planet. Sci. Lett.*, *278*, 243–256.
Hirth, G., and D. L. Kohlsted (2003), Rheology of the upper mantle and the mantle wedge: A view from the experimentalists, in Inside the Subduction Factory, *Geophys. Monogr. Ser.*, vol. 138, edited by J. Eiler, pp. 83–105, AGU, Washington, D. C.
Iwamori, H. (1998), Transportation of H_2O and melting in subduction zones, *Earth Planet. Sci. Lett.*, *160*, 65–80.
Iwamori, H. (2007), Transportation of H_2O beneath the Japan arcs and its implications for global water circulation, *Chem. Geol.*, *239*, 182–198.
Karato, S. I. (1989), Grain growth kinetics in olivine aggregates, *Tectonophysics*, *168*(4), 255–273.
McKenzie, D. (1969), Speculations on the consequences and causes of plate motions, *Geophys. J. R. Astron. Soc.*, *18*, 1–32.
Mibe, K., T. Fujii, and A. Yasuda (1999), Control of the location of the volcanic front in island arcs by aqueous fluid connectivity in the mantle wedge, *Nature*, *401*, 259–262.
Miller, K. J., W. L. Zhu, L. G. Montési, and G. A. Gaetani (2014), Experimental quantification of permeability of partially molten mantle rock, *Earth Planet. Sci. Lett.*, *388*, 273–282.
Mysen, B. O., and A. L. Boettcher (1975), Melting of a hydrous mantle: I. Phase relations of natural peridotite at high pressures and temperatures with controlled activities of water, carbon dioxide, and hydrogen, *J. Petrol.*, *16*, 520–548.
Pawley, A. R., and J. R. Holloway (1993), Water sources for subduction zone volcanism: New experimental constraints, *Science*, *260*, 664–667.
Peacock, S. A. (1990), Fluid processes in subduction zones, *Science*, *248*(4953), 329–337.
Peate, D. W., and C. J. Hawkesworth (2005), U series disequilibria: Insights into mantle melting and the timescales of magma differentiation, *Rev. Geophys.*, *43*, RG1003, doi:10.1029/2004RG000154.
Reubi, O., K. W. Sims, and B. Bourdon (2014), ^{238}U–^{230}Th equilibrium in arc magmas and implications for the time scales of mantle metasomatism, *Earth Planet. Sci. Lett.*, *391*, 146–158.
Riley, G. N., and D. L. Kohlstedt (1991), Kinetics of melt migration in upper mantle-type rocks, *Earth Planet. Sci. Lett.*, *105*(4), 500–521.
Schmidt, M. W., and S. Poli (1998), Experimentally based water budgets for dehydrating slabs and consequences for arc magma generation, *Earth Planet. Sci. Lett.*, *163*, 361–379.
Syracuse, E. M., and G. A. Abers (2006), Global compilation of variations in slab depth beneath arc volcanoes and implications, *Geochem. Geophys. Geosyst.*, *7*, Q05017, doi:10.1029/2005GC001045.
Syracuse, E. M., P. E. van Keken, and G. A. Abers (2010), The global range of subduction zone thermal models, *Phys. Earth Planet. Inter.*, *183*, 73–90.
Tatsumi, Y. (1986), Formation of the volcanic front in subduction zones, *J. Geophys. Res.*, *17*, 717–720.
Turner, A. J., R. F. Katz, and M. D. Behn (2015), Grain-size dynamics beneath mid-ocean ridges: Implications for permeability and melt extraction, *Geochem. Geophys. Geosyst.*, *16*, 925–946, doi:10.1002/2014GC005692.
Turner, S. P., B. Bourdon, C. J. Hawkesworth, and P. Evans (2000), ^{226}Ra-^{230}Th evidence for multiple dehydration events, rapid melt ascent and the time scales of differentiation beneath the Tonga-Kermadec island arc, *Earth Planet. Sci. Lett.*, *179*, 581–593.
Ulmer, P. (2001), Partial melting in the mantle wedge—The role of H_2O in the genesis of mantle-derived "arc-related" magmas, *Phys. Earth Planet. Inter.*, *127*, 215–232.
van Keken, P. E., B. Kiefer, and S. M. Peacock (2002), High-resolution models of subduction zones: Implications for mineral dehydration reactions and the transport of water into the deep mantle, *Geochem. Geophys. Geosyst.*, *3*(10), 1056, doi:10.1029/2001GC000256.

van Keken, P. E., et al. (2008), A community benchmark for subduction zone modeling, *Phys. Earth Planet. Inter.*, *171*, 187–197.
van Keken, P. E., B. R. Hacker, E. M. Syracuse, and G. A. Abers (2011), Subduction factory: 4. Depth-dependent flux of H_2O from subducting slabs worldwide, *J. Geophys. Res.*, *116*, B01401, doi:10.1029/2010JB007922.
Wada, I., and K. Wang (2009), Common depth of decoupling between the subducting slab and mantle wedge: Reconciling diversity and uniformity of subduction zones, *Geochem. Geophys. Geosyst.*, *10*, Q10009, doi:10.1029/2009GC002570.
Wada, I., K. Wang, J. He, and R. Hyndman (2008), Weakening of the subduction interface and its effects on surface heat flow, slab dehydration, and mantle wedge serpentinization, *J. Geophys. Res.*, *113*, B04402, doi:10.1029/2007JB005190.
Wada, I., M. D. Behn, and J. He (2011), Grain size distribution in the mantle wedge of subduction zones, *J. Geophys. Res.*, *116*, B10203, doi:10.1029/2011JB008294.
Wada, I., M. D. Behn, and A. M. Shaw (2012), Effects of localized hydration in the incoming plate, slab rehydration, and mantle wedge hydration on slab-derived fluid flux in subduction zones, *Earth Planet. Sci. Lett.*, *353 354–*, 60–71.
Wark, D. A., and E. B. Watson (1998), Grain-scale permeabilities of texturally equilibrated, monomineralic rocks, *Earth Planet. Sci. Lett.*, *164*, 591–605.
Wark, D. A., C. A. Williams, E. B. Watson, and J. D. Price (2003), Reassessment of pore shapes in microstructurally equilibrated rocks, with implications for permeability of the upper mantle, *J. Geophys. Res.*, *108*(B1), 2050, doi:10.1029/2001JB001575.
Wilson, C. R., M. Spiegelman, P. E. van Keken, and B. R. Hacker (2014), Fluid flow in subduction zones: The role of solid rheology and compaction pressure, *Earth Planet. Sci. Lett.*, *401*, 261–274.
Zhang, Z., and Z. Duan (2005), Prediction of the *PVT* properties of water over wide range of temperatures and pressures from molecular dynamics simulation, *Phys. Earth Planet. Inter.*, *149*(3), 335–354.
Zhu, W., and G. Hirth (2003), A network model for permeability in partially molten rocks, *Earth Planet. Sci. Lett.*, *212*(3), 407–416.